# Process Monitoring and Estimation of Material Properties of Additively Manufactured Components Using Model-Based Inversion of Process Compensated Resonance Testing Data

**Julieanne Heffernan**
Vibrant,
Albuquerque, NM 87113
e-mail: jheffernan@vibrantndt.com

**Alexander Mayes**
Vibrant,
Albuquerque, NM 87113
e-mail: amayes@vibrantndt.com

**Niklas Höhn**
Vibrant GmbH,
65604 Elz, Germany
e-mail: nhoehn@vibrantndt.com

**Martin Bach**
Airbus Helicopters GmbH,
Donauwörth 86609, Germany
e-mail: martin.bach@airbus.com

**Ira Widmayer**
Airbus Helicopters GmbH,
Donauwörth 86609, Germany
e-mail: ira.widmayer@airbus.com

**Eric Biedermann**
Vibrant,
Albuquerque, NM 87113
e-mail: ebiedermann@vibrantndt.com

**Leanne Jauriqui**
Vibrant,
Albuquerque, NM 87113
e-mail: ljauriqui@vibrantndt.com

*Certification of additively manufactured (AM) parts and qualification of AM processes, suppliers, and machines for aerospace applications involve significant mechanical testing, cost, and time. The AM community requires capabilities for fast, affordable, and effective certification and qualification. These capabilities include rapid component and model validation, characterization of process and geometry impact on material properties, build and process monitoring, and effective nondestructive evaluation (NDE). Process compensated resonance testing (PCRT) uses the resonance frequencies of a component to rapidly detect defective parts, monitor build and processes and post-processing, characterize material properties, and can be used as a basis for model validation. This study examines the use of PCRT model-based inversion to nondestructively determine the material properties of as-built titanium AM components. Over 100 samples were printed with intentional variations in build parameters, with the intention to produce generic "acceptable" and "unacceptable" components. PCRT modeling tools were then used to train the inversion code algorithms. The model-based inversion estimated the elastic properties of the as-built parts as well as a residual fit error, identifying several components with outlying properties. Parts were then mechanically tested, and the outliers were confirmed. As PCRT model-inversion is a powerful NDE method, several examples are described showing how inversion results can augment traditional AM inspection techniques.* [DOI: 10.1115/1.4054144]

*Keywords: aerospace engineering, damage classification, manufacturing processes, materials testing, testing methodologies, vibrations*

## 1 Introduction

Additively manufactured (AM) components are being used increasingly in more critical applications. Certification of AM parts and qualification of AM processes, suppliers, and machines for aerospace applications involve significant mechanical testing, cost, and time. Traditional nondestructive evaluation (NDE) methods are used in AM components for examining surface and internal defects. Typical surface inspections include visual inspection, penetrant inspection (PT), surface roughness, and dimensional inspections via gauges or coordinate measurement machines. Subsurface and internal inspections include radiography (RT), ultrasonic (UT), and computed tomography (CT) methods to name a few [1–3]. UT and PT can be limited in their effectiveness because of complex geometries, surface roughness, and pre-machining variation in parts after initial removal from build plates. While RT and CT methods are not limited by the complex part geometries, layer-level AM defects are often harder to resolve due to the resolution levels of the components [1]. Other process monitoring tools may evaluate the quality of the feedstock powder prior to the build or use optical or thermal sensors to attempt to detect deviations during the build [2]. Feedstock powder evaluations will detect material deviation prior to the build and avoid the time and cost of building with bad powder, but it cannot account for build process variations that can produce an unacceptable part [4]. Optical and thermal sensing during the build can also detect some geometric and material state deviations, opening the possibility for aborting a build with defects or possibly salvaging the build with a correction to the process [5]. However, the final product of the build must still be checked against acceptability criteria to ensure the component is fit for use, especially if the process has been interrupted or altered to salvage a build.

Volumetric inspection methods, such as process compensated resonance testing (PCRT), can inspect the full range of geometric complexity in parts made by AM while also detecting variation in partial state produced by AM process variations [6–8]. PCRT, via swept sine input, offers significant advantages for the AM community through the collection and analysis of the resonance frequency data for each part in an AM build. Variations in the component's material state, and by extension mechanical performance, caused by process and/or powder variation will manifest as differences in the resonance frequencies, also called natural frequencies, of a part. Historically, applications of PCRT have evaluated parts by comparing a part's resonance to a database of spectra recorded from a training population of characterized acceptable and unacceptable components. PCRT has been used similarly for AM monitoring [6] and has been identified as one of only two NDE methods

Manuscript received September 30, 2021; final manuscript received March 15, 2022; published online April 8, 2022. Assoc. Editor: Hoon Sohn.

that can inspect the full range of geometric complexity in parts made by AM [8].

To improve PCRT capabilities for characterizing material states, PCRT research has focused on developing modeling and inversion capabilities to better predict the effects of changes in material, geometry, and damage states on the resonance frequencies [9]. Historically, resonance inversion methods use an energy minimization technique that finds resonances of a solid body by approximating solutions of the mechanical Lagrangian within resonance ultrasound spectroscopy (RUS) [10,11]. While this approach is computationally inexpensive, it is limited to simple, elastically homogenous geometries such as spheres, rectangular parallelepipeds, and cylinders. To perform inversion of more complex geometries, material characteristics, and damage states, a finite element method (FEM) modeling approach can be implemented. To reduce the computational time of FEM inversion, surrogate models can be improved using different sampling schemes and model approaches [12]. PCRT model-based inversion, supplemented by FEM results, has demonstrated the determination of elastic material properties, crystallographic orientation, and damage states in coupons and multiple geometries made from titanium, steel, and nickel-based alloys [13–15].

The goal of this study was to demonstrate the ability of PCRT model-based inversion to estimate material properties of AM Ti–6Al–4V (Ti-64) components built under a variety of conditions. An FEM population of as-built cylinder coupons was used to train an inversion model. Resonance frequencies of printed cylinders were measured with a PCRT fixture and the data feed into the inversion code loop. The outputs of the inversion code were the best-fit material property estimations of the printed cylinders. Mechanical testing confirmed PCRT inversion estimations of parts with suboptimal properties.

## 2 Materials and Methods

**2.1 Initial Modeling Efforts.** Using FE simulations, a series of forward models of AM cylinders were created to act as a training set for the inversion code. A block Lanczos solver was used with the FEM code ANSYS to generate the resonance frequencies for each simulation. A mesh sensitivity study was performed to optimize the mesh for accuracy and computational time. The study ran modal analyses the baseline Ti-64 cylinder specimen with successively finer meshes and compared the frequency error between each run until a convergence criterion was met. The mesh at convergence comprised approximately 150,000 tetrahedral mesh elements. Figure 1 shows an example of two modeled resonance modes of the cylinder (showing an expanded view of torsional and bending shapes that can occur) with the overlayed mesh of the AM cylinder

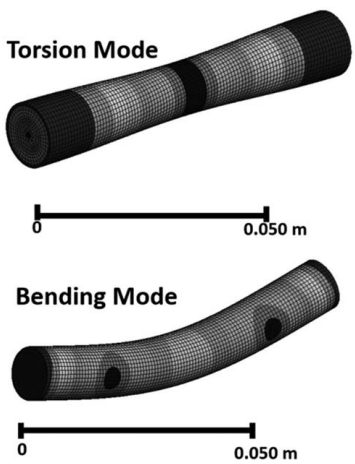


**Fig. 1 Example torsion and bending mode from FEM of AM cylinder**

used. Next, a series of one-factor-at-a-time (OFAT) FEM simulations were performed with the cylinder model. The simulations varied individual geometric and material parameters to evaluate their effect on the specimen resonance spectra and establish a normal distribution of parameter variation versus resonance frequencies. Figure 2 shows the frequency changes for the geometric and material changes simulated in the AM cylinder. The largest change in frequencies occurred with variations in Young's modulus ($E$), followed by Poisson's ratio ($\nu$), and density ($\rho$) as estimated from the expected variations that would be present on the printed cylinders. Because the length and diameter of the AM cylinders can vary slightly (depending on machine tolerances and cutoff of electrical discharge machining (EDM) wire), variations in length ($L$) and diameter ($D$) of the cylinders were considered and were shown to have a strong influence on the individual resonance mode shapes or pattern between mode shapes. Due to the build settings, residual support material was often left on the bottom edge of one side of each cylinder creating a rounded edge on one end. When modeling the rounded edge, shown as a black solid line in Fig. 2, the effect on the resonance frequencies was less than 0.3% across all modes. As this was less than the effects of $L$, $D$, or material properties on resonance frequencies, the rounded edges were not included as factors in the inversion design space.

**2.2 Model-Based Inversion.** Process compensated resonance testing model-based inversion determines the material state of a component by fitting a modeled prediction of resonance frequencies, based on known material state information, to the component's measured resonance spectra. This inversion process is summarized in Fig. 3. Similar inversion processes used in this study are described in more detail in Ref. [9].

The measured resonance frequencies of each part, measured with PCRT (described in Sec. 2.4), and an initial guess of their material properties were passed to the inversion loop. The frequencies from 44 of the parts measured resonance modes were used along with an initial guess of $E$ and $\nu$ of an isotropic Ti-64 alloy. Additionally, the masses and dimensions of each part were added to the inputs in order to reduce the number of unknown variables for the inversion.

In order to create a robust training set of parts for the inversion code, a design space was created that included a population of 221 cylinders, sampled in a Latin hypercube manner, to encompass the expected variation be printed across the AM builds. Table 1 describes the parameters used in the modeled design space training set.

Next, the inversion loop took the initial property guesses and interpolated within the FEM modeled design space that best corresponded to those guesses. The resulting interpolated frequencies were then compared to the measured sample frequencies and the root-mean-square of the residual errors (RMSEs) were calculated across 44 resonance modes and passed to the optimization routine. The optimization routine made changes to the parameter values based until a best-fit solution was found that met the convergence criteria. The convergence criteria here included an analysis of the RMSE, boundary limits for the independent variables (material/dimensional), and the change (or lack of change) in the results from each iteration. Non-linear least-squares estimation is not guaranteed to multiple repetitions of each inversion performed using different initial values. Initial values were chosen pseudo-randomly using Latin hypercube sampling to ensure that the full range of parameter values in the given bounds was represented [16]. Finally, the best-fit solution was then chosen as whichever repetition had the lowest RMSE. The resulting RMSE, best-fit solution of $E$, and best-fit value of $\nu$ of the measured spectra were output from the code.

**2.3 Heat Transfer Simulations to Estimate Desired Process Parameters.** The intent in this study was to build parts with a range of mechanical properties to simulate rages of properties an end user may deem as acceptable and non-acceptable. Parts intended to have

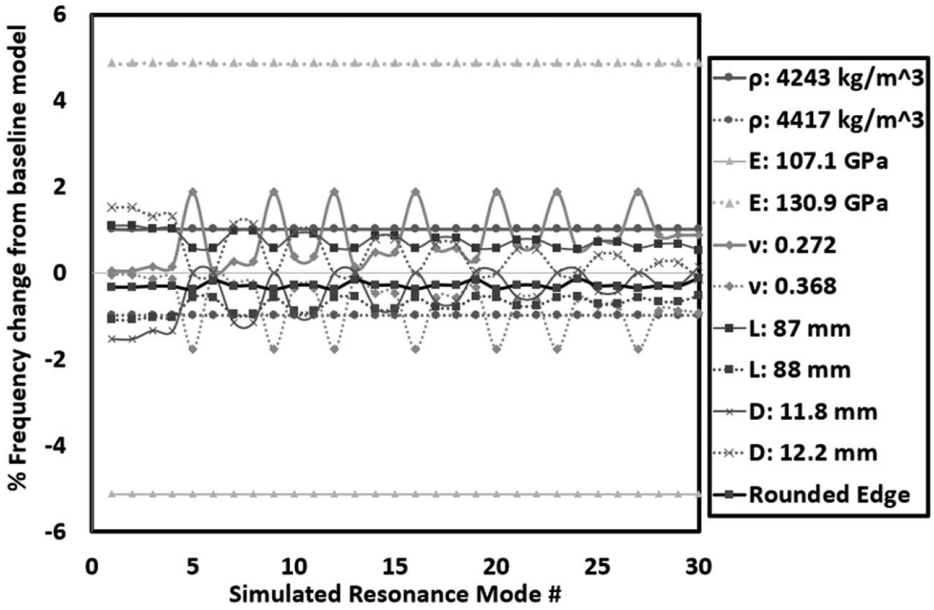


**Fig. 2 OFAT sensitivity analysis of frequency variation**

unacceptable tensile results were built with build process variations to produce lack of fusion (LOF), porosity due to undermelting, or keyhold porosity due to overheating. In order to estimate the optimum processing windows for these conditions, a series of 10 simple 2D finite difference heat diffusion simulations were conducted on a Ti-64 alloy by the part manufactures on a proprietary software. The simulations varied the simulated laser power (LP) from 60% to 100% (LP60–LP100) and layer thickness (LT) from 60 to 120 $\mu$m (LT60–LT120). The laser diameter (100 $\mu$m), hatch spacing (120 $\mu$m), and printing path of the components were held constant in these simulations to minimize variables in the as-built components. The simulations considered the heat transfer in a 2D slice while the effect from the bottom layers was not considered. Also, simulations also considered heat loss, convection, and radiation heat loss. The associated energy densities of each simulation were calculated, and the results for 10 of these simulations are shown in Fig. 4. The simulations were evaluated for porosity and how well the samples melted. Overheating maps confirmed that simulations 1, 2, 3, and 4 showed excellent melting conditions and were less likely to have any LOF as well as keyhole porosity issues. Simulations 6 and 7 with energy densities less than 19 J/mm$^3$ had the lowest laser power settings and showed the poorest density and lack of melting. The rest of the samples were considered to have borderline melting conditions. The simulation settings for acceptable and unacceptable melts were used as guidelines for the build settings in the as-built parts to manifest likely acceptable and unacceptable mechanical properties. For example, build settings were used to match simulation #6, LP of 60%, and a layer thickness of 60 $\mu$m, with the expectation this would produce poor porosity in the sample and thus have lower mechanical properties than the other groups. It was noted by the manufacture, however, that any post operations such as hot isostatic pressing (HIP) on the components may reduce or completely eliminate the porosity of the samples.

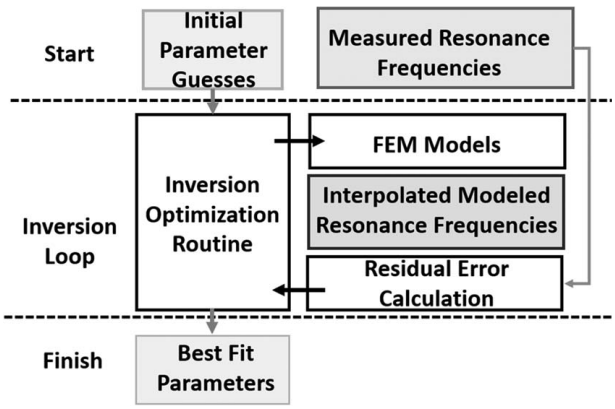


**Fig. 3 Diagram of PCRT model-based inversion**

**2.4 As-Built Samples and PCRT Data Collection.** Table 2 describes the 140 titanium cylinders built on a four laser powder bed diffusion (PBD) machine. Cylinders were 87.3 mm long by 11.95 mm in diameter. Parts were built within six build setting groups with intentional variation in LT from 60 to 120 $\mu$m or variation in LP from 60% to 100% within each group. The group names are listed in Table 2 along with the associated laser power and layer thickness settings built for each group. For example, the build group LT80 consisted of 20 parts with build settings of LT of 80 $\mu$m and an 88% LP. While most parts were produced evenly over several builds, all parts from the LT80 group came from a single build and were approximately 0.8 mm (1%) longer than the cylinders from all the other builds. All part mass measurements were taken with a scale and dimensions were measured with calipers. In typical part production, the cylinders would have been blasted, HIP'ed, and etched. However, the populations for this work were not HIP'ed so as not to eliminate any porosity that occurred due to the build settings.

Process compensated resonance testing spectra were collected on each cylinder on a standard PCRT engineering fixture shown in Fig. 5. One piezoelectric transducer induced a swept sine wave across the frequency range of interest (Drive), two transducers

**Table 1 Model input parameters for FEM design space**

| | Density (kg/m$^3$) | Young's modulus (GPa) | Poisson's ratio, $\nu$ | Length (mm) | Diameter (mm) |
|---|---|---|---|---|---|
| Baseline | 4330 | 119 | 0.32 | 87.5 | 12 |
| Lower bound | 4243.4 | 107.1 | 0.272 | 87 | 11.8 |
| Upper bound | 4416.6 | 130.9 | 0.368 | 88 | 12.2 |

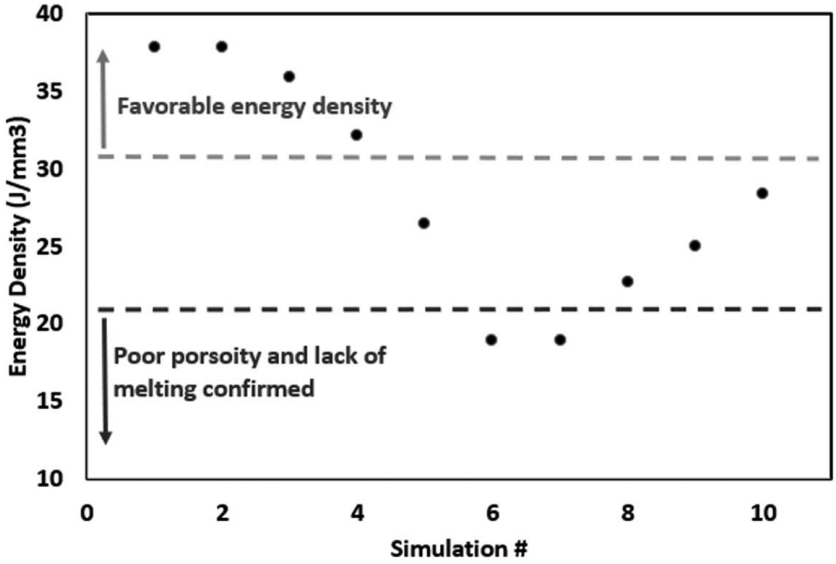


**Fig. 4 Simulated energy densities of heat transfer simulations**

were used to measure the response (Ch 1 and Ch 2), and one transducer was used to provide stable support of the cylinder. The repeatability of the resonance measurements on the fixture was also studied by making 30 repeat measurements of the same part. Multiple measurements included variation in part temperature and placement of the fixture (including part rotation). The measurement repeatability of the frequencies for most modes was between 0.02 and 0.06 (standard deviation, %). The repeatability of this data was considered very good. Scanning from 11 to 250 kHz took approximately 2 min per part. Results were added to a database of all components and 87 individual resonance modes of each part were evaluated. Out of the 87 modes, 44 measured resonance modes, corresponding to ANSYS FEM modeled modes, were identified and feed as inputs to the inversion code. While not used for inversion investigation here, PCRT data were also taken on each machined dogbone before tensile testing.

To provide more direct information as a comparison to the PCRT and model-based inversion results of the coupons, tensile testing was performed. A 20 kip Instron tensile screw-driven rig was used with a strain rate through 0.2% yield of 0.0127 cm/min at 24 °C. Results included a reporting of each part's ultimate tensile strength, yield strength, and % elongation. One hundred and ten of the cylinders were machined to ASTM E-8 compliant dogbones for tensile testing [17]. Several cylinders from each build group were not machined and a total of 30 samples were retained for future microstructure evaluations, heat treatment, and other NDE studies.

## 3 Results and Discussion

**3.1 Model-Based Inversion Results.** Figure 6 shows the best-fit inversion results of $E$ and $\nu$ along measured cylinders for all 140 cylinders created. In the majority of parts, and those in the reference set, the average $E$ was 119.5 GPa and the average $\nu$ was 0.321. These values are consistent with those from a cast titanium Ti-64 alloy. The RMSE across all 44 resonance modes calculated for the cylinders is shown in Fig. 7. Typical RUS inversion results with RMSE up to 0.5% constitute a good fit [15] so the RMSE <0.3% here gives increased confidence in the parameter estimations output from inversion. Additionally, confidence in the modeled and inversion results requires a good match between the physical and simulated resonance frequencies. Figure 8 shows the % frequency difference between the FEM model, using best-fit inversion properties, compared to measured frequency

**Table 2 As-built parameters used for AM component builds**

| Group name | Laser power (LP) (%) | Layer thickness (LT) ($\mu$m) | Number of parts |
|---|---|---|---|
| Reference | 100 | 60 | 40 |
| LP85 | 85 | 60 | 20 |
| LP70 | 70 | 60 | 20 |
| LP60 | 60 | 60 | 20 |
| LT120 | 100 | 120 | 20 |
| LT80 | 88 | 80 | 20 |

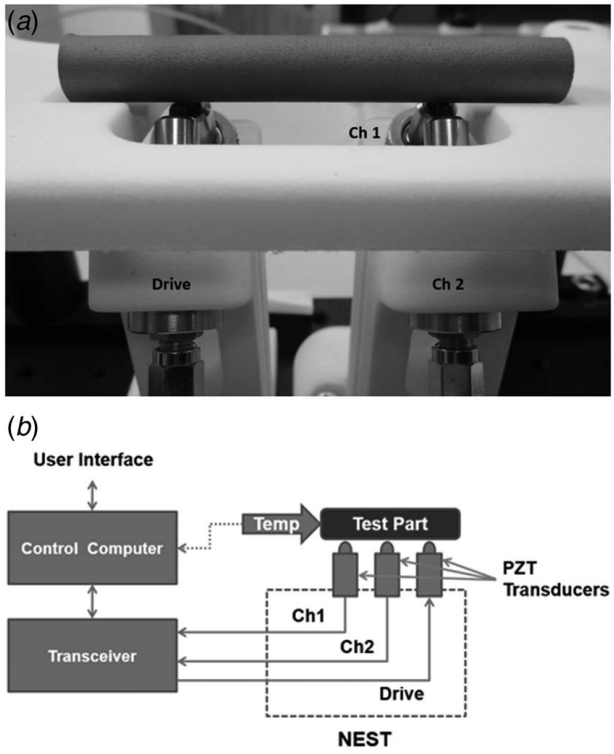


**Fig. 5 Cylinder on PCRT engineering fixture (*a*) and PCRT system schematic (*b*)**

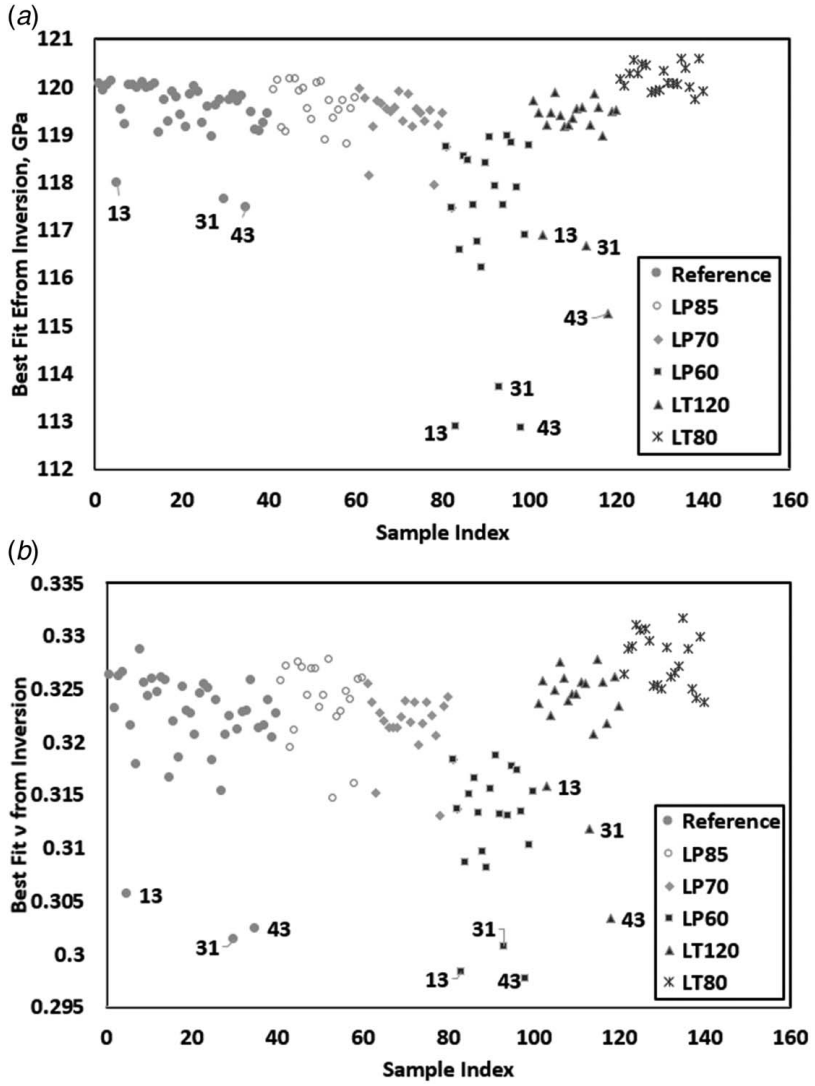


**Fig. 6 Best-fit model-based inversion results of (*a*) *E* and (*b*) ν for AM cylinders**

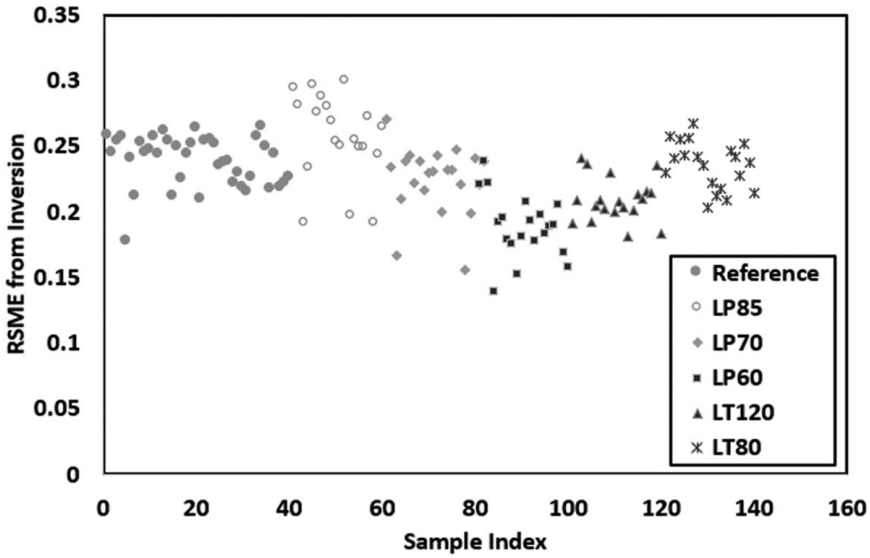


**Fig. 7 RMSE for model-based inversion fits for AM cylinders**

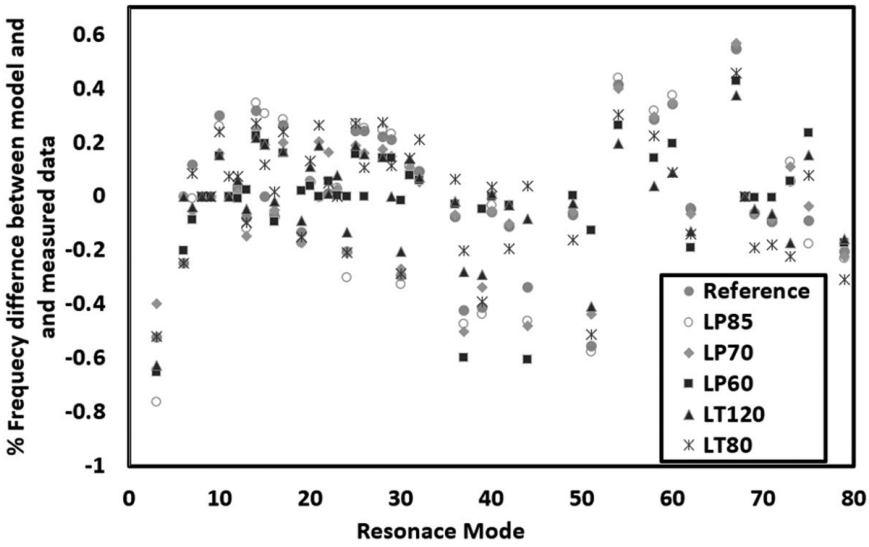


**Fig. 8 Percentage difference between FEM model, using best-fit inversion properties, and measured spectra from one part in each build group**

resonance modes for six cylinders (one from each build group). The match was considered good as the majority of modeled frequencies showed a very close measured frequency match (±0.3%).

Several inversion result outliers, produced across multiple builds within each group, were found to be printed at the same build plate location. For instance, parts produced in positions 13, 31, and 43 are labeled within the reference, LP60, and LT120 groups, in Figs. 6 and 7. The inversion results for these parts were outliers when compared to the results from the rest of their respective groups. However, the RMSE indicates a good parameter estimation of these properties. Also, at a lower laser power, for a given speed, the PBD melt pool will be smaller. This in turn reduces the chance of turbulence and splatter, and the entrainment of neighboring powder on the parts. However, if the LP is too low, it could lead to LOF defects as the laser cannot penetrate deeply enough to fully melt the powder layer and the top surface of solid metal below it. While parts produced from 88% to 100% LP had overlapping properties, parts produced with the lowest laser power LP60 had the lowest values of $E$ and $\nu$ as well as the largest spread of variation across the parts. Similarly, several of the thick powder layer LT120 parts also had low $E$ and $\nu$ inversion results. This is consistent with potential LOF defects in these groups.

**3.2 Mechanical Results.** Figures 9–12 show the mechanical results of $E$, tensile strength, yield strength, and % elongation of the machined AM dogbones machined from the cylinders. Of the 110 samples sent for testing, one sample from the LP60 group (position 30) was reported as invalid and the results are not reported. The outliers identified by inversion were found to be outliers in one or more of their mechanical properties. For example, parts in build plate positions 13, 31, and 43 from the LP60, LT120, and reference groups were outliers with low tensile strength compared to the rest of the population and parts within their group. Position 13 from the reference group also had mechanically lower yield strengths and % elongation compared to the rest of the reference parts. Parts in the LP60 and LT120 groups were found to have the largest spread of mechanical values, consistent with inversion results. Nominal Ti-64 alloys are reported with $E$ values ranging from 90 to 120 GPa and tensile strength values ranging 90–140 GPa [18].

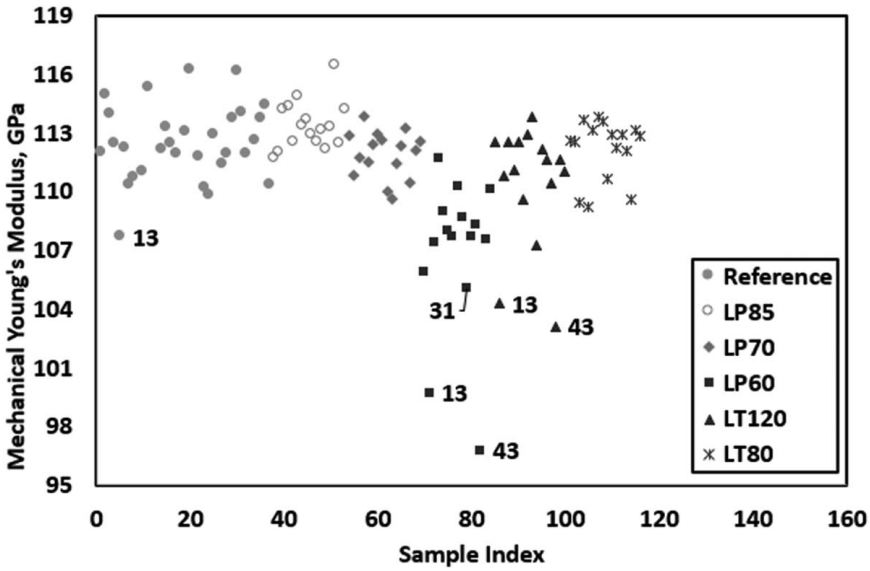


**Fig. 9 Experimental *E* results of the AM dogbones**

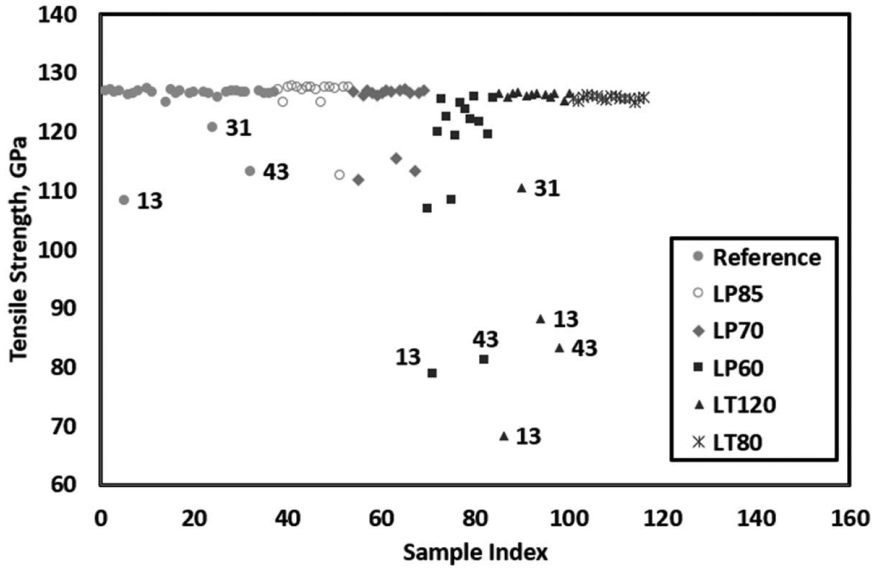


**Fig. 10 Tensile strength results of the AM dogbones**

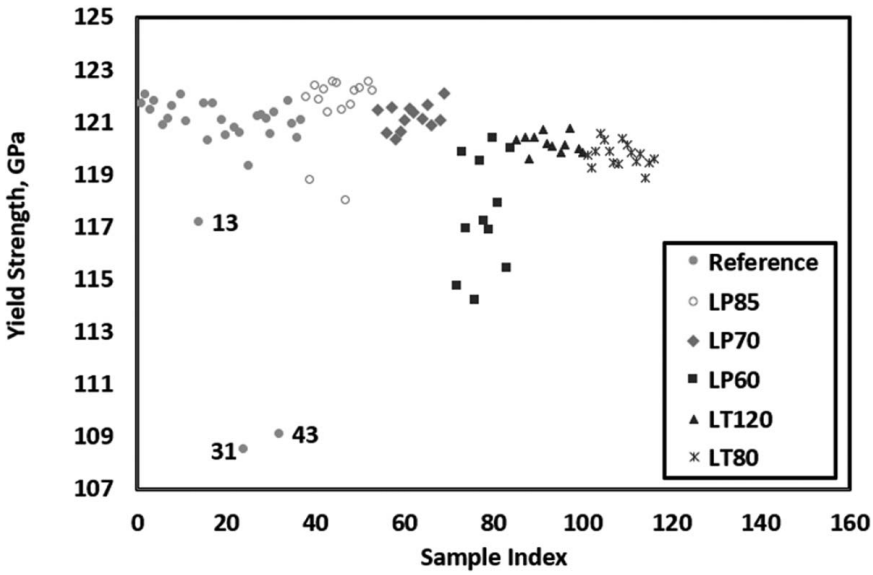


**Fig. 11 Yield strength results of the AM dogbones**

The printed parts showed $E$ values within this range for all parts. Parts printed at positions 13 and 43 in groups LT120 and LP60 had slightly lower tensile strength values.

Figure 13 shows the inversion results of modulus compared to the mechanical calculations of $E$. Overall, the inversion estimates were 5% lower than the mechanical calculations. Part of this offset can be attributed to an expected standard deviation of ±5% for elastic modulus measurements from tensile testing [19,20]. Even with this offset, a linear correlation is present between the inversion and mechanical calculations of $E$ with an $R^2$ value of 0.8058 as shown in Fig. 13.

The scope of this project limited the inversion code to fitting parts only with dimensions, mass, $E$, and $\nu$ and assumes isotropic properties. Not all as-built AM materials will be isotropic, and it is unknown if the parts in these builds have additional alignment characteristics perpendicular to the build direction. Future work can estimate microstructure on some components by further NDT or destructive material analysis of the 30 of AM cylinders that were not machined into dogbones or tensile tested. The inversion code is also blind to other part properties that can affect the mechanical results, such as residual stress on the outside of the part. For example, solidification conditions during an AM build can cause variation in the Ti-64 grain structure, texture, and material properties on the outside surface of the part compared to the center [21]. While microstructure of the parts were not examined in this study, however, the measured mechanical trends are very similar to the trends shown within the part's resonance response. The overall model to measure match of the parts was considered a good fit (Fig. 8) and the inversion RMSE across all resonance modes was less then <0.3% for all parts. Typical RUS inversion results with RMSE up to 0.5% constitutes a good fit [15], so the lower value in this study gives increased confidence in the material parameter estimations.

## 4 Discussion: Use of Model-Based Inversion Results

The rapid range and complexity of AM processes add many challenges to developing physics-based models with repeatability and

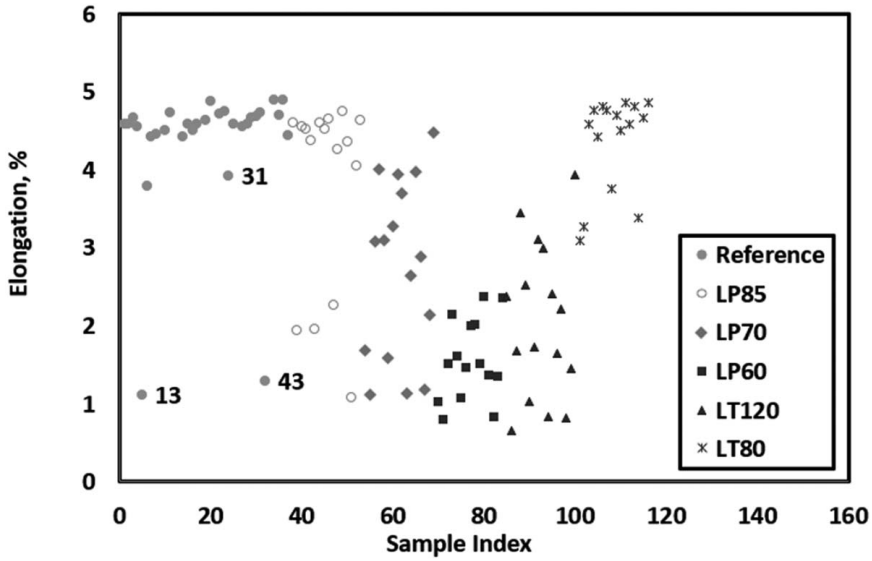


**Fig. 12 Percentage elongation results of AM dogbones**

reproducibility of predictions across varying processes and process parameters. A significant advantage in PCRT model-based inversion is the ability to quickly output the material properties on each component. Inversion can be used in a similar way through the entire production process (heat treatment, machining, etc.) and service life of the components as variations in those processes will affect the components' material states. The material properties can act as inputs for a component's physics-based model that can be used in model-based fatigue, fracture, and microstructure part qualification. Additionally, the effectiveness of resonance frequency residual error has been shown as a means of measuring model fidelity [9].

Aside from modeling, inversion results can provide NDE for enhanced AM part characterization, qualification, and process monitoring. In an operational context, the parts would be removed from the build plate, scanned with PCRT for select frequencies, and have their best-fit inversion results displayed within seconds. An operation inspection would have limits placed around the acceptable and unacceptable inversion results. Determining the limits would be based on what the users deem acceptable or not. For example, Fig. 14 shows a representation of a pass/fail PCRT inversion inspection based on the inverted best-fit $E$ values. Any components with modulus values inverted within the specification limits pass the inspection. Components with modulus values outside the specification limits fail the inspection. For this example, limits have been set arbitrarily between $E$ values of 117.5 and 121 GPa as this encompasses variation within 95% of the reference set of parts. This inspection fails several of the outliers as well as half of the LP60 group components.

Another characterization method that can be used in the filed would be to evaluate the parts that are being produced in relation to the build map and or related process settings. Detecting defective material properties in the post-build state allows those parts to be removed from the process stream without spending additional resources on additional machining, heat treatments, or other costly post-processing. For example, Fig. 15 shows the build map of the AM parts in this study. Each square represents a part position on the $X$ and $Y$ plane build map. The number in each square shows the inverted $E$ results found through PCRT. The shade of each square shows the relative values of $E$ within the build plate. As shown, the center of the plate produced parts with lower inverted

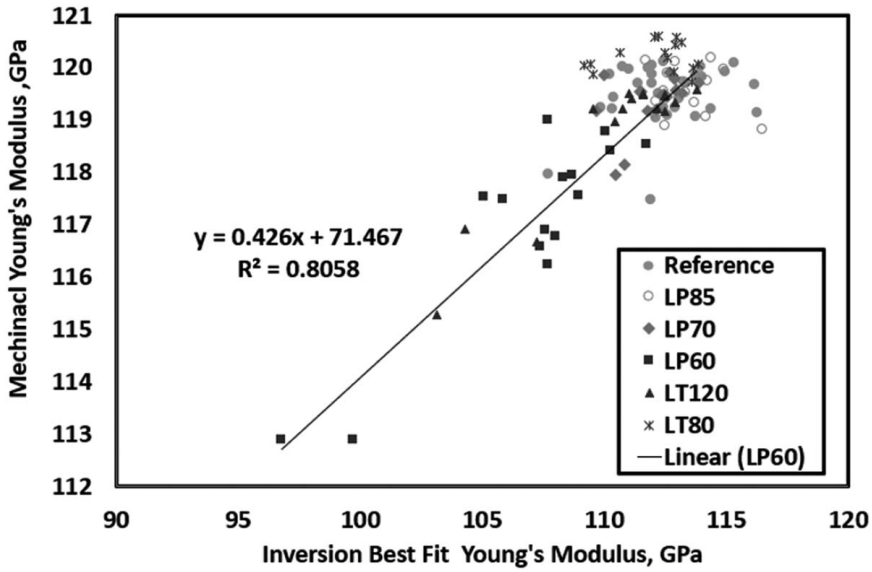


**Fig. 13 Inversion best fit versus mechanical reporting's of *E***

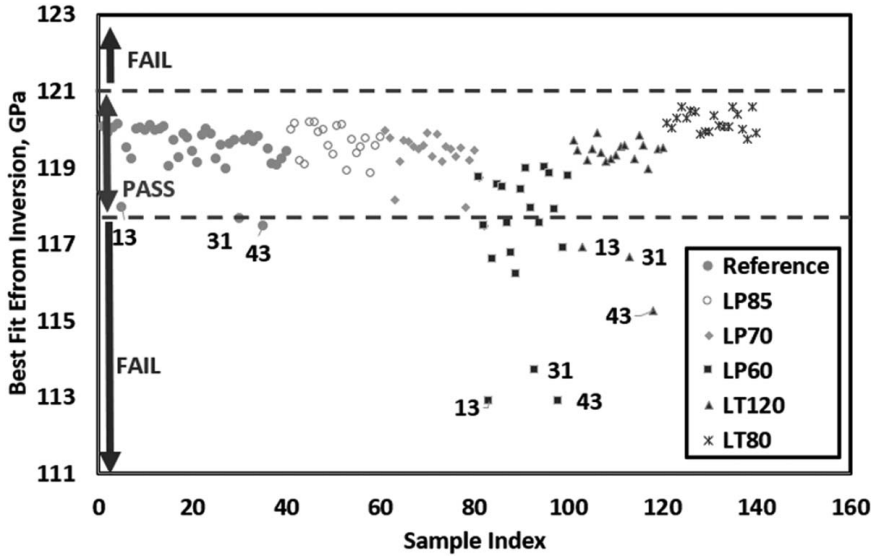


**Fig. 14 Example of inversion-based run chart inspection**

*E* values. It was suspected that turbulent air flow in the middle of the plate was causing a cooling rate change, thus affecting the microstructure and resulting modulus values of the part. With this knowledge, the AM manufacturer can decide if they need to change the build settings or build map locations of parts to eliminate or avoid the problem areas.

Model-based inversion can also allow insight into part characterizations not found with traditional PCRT analysis such as PCRT *Z*-score calculations. The *Z*-score analysis begins with logging resonance spectra data for parts within a database and designating a subset of these parts as a reference set of nominal acceptable properties. Equation (1) provides the calculation of the *Z*-score ($Z_{ij}$) for a given resonance frequency ($FQ_{ij}$). For each mode of vibration $j$, the average frequency across all parts in the reference set, $\overline{FQ}_j$, is calculated. Then, for each part/mode combination ($ij$) in the database, including parts outside of the reference set, a *Z*-score $Z_{ij}$ is calculated from Eq. (1) where $n$ is the number of modes of vibration in the database:

$$Z_{ij} = \frac{FQ_{ij} - \overline{FQ}_j}{\sqrt{\sum_{j=1}^{j=n} (FQ_{ij} - \overline{FQ}_j)^2/(n-1)}} \tag{1}$$

The *Z*-score average, $\bar{Z}_i$, for each part is then calculated by averaging the $Z_{ij}$ values across all the modes for each part. The *Z*-score average calculation uses expression (2):

$$\bar{Z}_i = \frac{\sum_{j=1}^{j=n} Z_{ij}}{n} \tag{2}$$

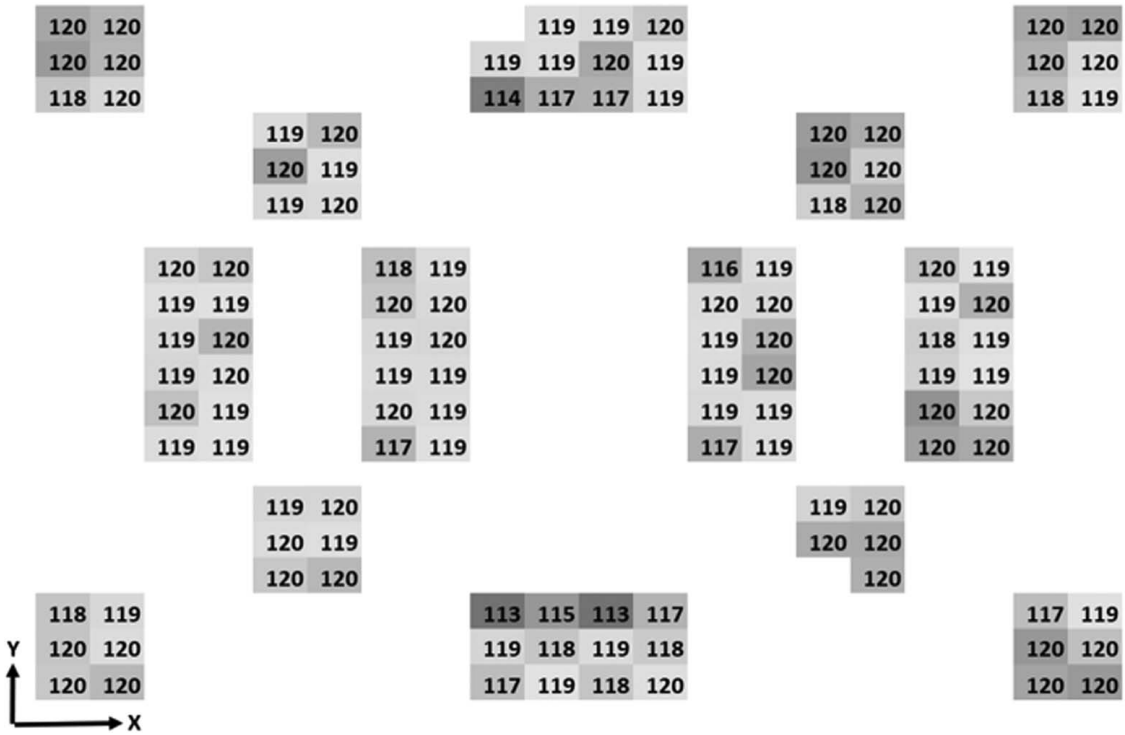


**Fig. 15 Color scaled best-fit inversion *E* results (GPa) of each part overlayed with the AM build map**

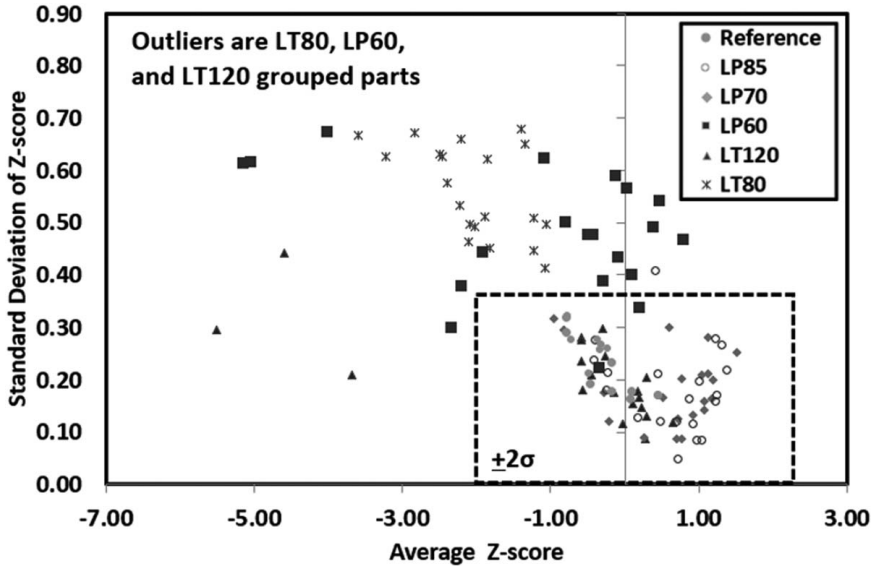


**Fig. 16 PCRT *Z*-score outlier inspection (without inversion integration)**

Finally, the *Z*-score standard deviation is calculated from the $Z_{ij}$ values and $\bar{Z}_i$ for each part. The *Z*-score standard deviation calculation uses expression (3):

$$Z_{\text{stdev},i} = \sqrt{\frac{\sum_{j=1}^{j=n} (Z_{ij} - \bar{Z}_i)^2}{(n-1)}} \tag{3}$$

The *Z*-score standard deviation is then plotted against the *Z*-score average in a scatter plot. The *Z*-score average quantifies bulk frequency variation in the spectra (all modes shifting to lower or higher frequencies together) and often correlates to bulk material properties like Young's modulus. The *Z*-score standard deviation quantifies pattern variation in the population's resonance spectra. If the modes of a part's spectrum have some modes with higher frequencies and some with lower frequencies relative to the rest of the population, it will have a higher *Z*-score standard deviation value. The *Z*-score standard deviation often correlates to localized material state variations or defects.

Figure 16 shows a PCRT *Z*-score characterization of the components in this study, developed in accordance with an outlier screening inspection described by ASTM E3081 [22]. Arbitrary limits ($\pm 2\sigma$) were place around the *Z*-score so that a part with an average *Z*-score or *Z*-score standard deviation outside of the limit will fail inspection. This inspection fails outlier parts from groups LP60 and LT120. This is consistent with the fact that they have unacceptably low modulus and tensile strength. Yet, this inspection also fails all the LT80 parts as discussed in Sec. 2.4; the LT80 parts were approximately 0.8 mm (1%) longer than the rest of the cylinders produced due to how they were cut from the build plate. Because they were heavier and longer than the majority of the parts, their resonances were shifted causing them to fail inspection. In most AM applications, this is not as critical because often parts go for final machining to remove any residual material or support structure remnants before they are put in use. Because geometric and mass variation was accounted for within the FEM design space used to train the inversion code, inversion did not flag these parts as outliers. If it is desirable to identify these parts, PCRT pass/fail inspections without inversion can be configured, as described by ASTM E3081 [22].

## 5 Conclusion

This study generated an FEM trained inversion model to measure material properties of AM titanium parts. Good model to measure frequency matches as well as low RMSE fits between the inversion model and measured resonance frequencies of the parts gave increased confidence to the accuracy of the best-fit material properties. Inversion identified parts that were likely to have underperforming properties, and this was confirmed with tensile testing. The inversion best-fit properties of $E$ for the AM parts were within 5% of the absolute measured tensile measurements. The study also presented several examples how model-based inversion results can be integrated into and augmented with traditional NDE AM inspection techniques for field service inspection as part of AM part certification or AM processes qualification. Future work will include inversion studies confirmed with microstructure evaluations as well as inversion of more complex parts, damage states, and material HIP'ed parts. Investigations will also continue on how the inversion results can act as inputs into physics-based models of parts, allowing more rapid model validations and build parameter optimizations in the field.

## Acknowledgment

This work was developed under a corporative agreement between Vibrant, Materialize, and Airbus Helicopters under the program Additive Manufacturing Material Properties from Resonance Data (AMMARES). The authors would like to thank additional team members at Vibrant, Vibrant GmbH, Materialize, and Airbus Helicopters for their input on providing samples, simulations, data collection, and data analysis.

## Nomenclature

$D$ = diameter
$E$ = Young's modulus
$L$ = length
ASTM = ASTM international
Ti-64 = titanium alloy Ti–6Al–4V
$\nu$ = Poisson's ratio
$\rho$ = density

## References

[1] Weaver, G., 2018, "Additive Manufacturing and Inspection Difficulties," Qual. Mag., https://www.qualitymag.com/articles/94838-additive-manufacturing-and-inspection-difficulties

[2] McCann, R., Obeidi, M. A., Hughes, C., McCarthy, É., Egan, D. S., Vijayaraghavan, R. K., Joshi, A. M., et al., 2001, "In-Situ Sensing, Process

Monitoring, and Machine Control in Laser Power Bed Fusion: A Review," Addit. Manuf., **45**, p. 102058.
[3] ASTM E3166, 2020, "Standard Guide for Nondestructive Examination of Metal Additively Manufactured Aerospace Parts After Build," ASTM International, www.astm.org
[4] Cunha, F., Santos, T., and Xavier, J., 2021, "In Situ Monitoring of Additive Manufacturing Using Digital Image Correlation: A Review," Materials, **14**(6), p. 1511.
[5] Foster, B. K., Reutzel, E. W., Nassar, A. R., Hall, B. T., Brown, S. W., and Dickman, C. J., 2015, "Optical, Layerwise Monitoring of Powder Bed Fusion," 26th Annual International Solid Freeform Fabrication Symposium, SFF-2015, http://utw10945.utweb.utexas.edu/sites/default/files/2015/2015-24-Foster.pdf
[6] Vibrant Corporation, 2018, "PCRT Resonance Solutions—Additive Manufacturing," White Paper, https://www.vibrantndt.com/advanced-technology/
[7] Schwarz, J., Saxton, J., and Jauriqui, L., 2005, "Process Compensated Resonant Testing in Manufacturing Process Control," Mater. Eval., **63**(7), pp. 736–739.
[8] Todorov, E., Spencer, R., Gleeson, S., Jamshidinia, M., and Kelly, S., 2014, "America Makes: National AM Innovation Institute (NAMII)—Project 1: Nondestructive Evaluation (NDE) of Complex Metallic AM (AM) Structures—June 2014 Interim Report. AFRL-RX-WP-TR-2014-0162."
[9] Mayes, A., Heffernan, J., Jauriqui, L., Livings, R., Biedermann, E., Aldrin, J., Goodlet, B., and Mazdiyasni, S., 2019, "Process Compensated Resonance Testing (PCRT) Inversion for Material Characterization and Digital Twin Calibration," AIP Conf. Proc., **38**, p. 020019.
[10] Migliori, A., Sarrao, J., Visscher, M. W., Bell, T., Lei, M., Fisk, Z., and Leisure, R., 1993, "Resonant Ultrasound Spectroscopy Techniques for Measurement of the Elastic Moduli of Solids," Phys. B, **183**(1–2), pp. 1–24.
[11] Migliori, A., and Sarrao, J. L., 1997, *Resonant Ultrasound Spectroscopy*, Wiley, New York.
[12] Aldrin, J. C., Mayes, A., Jauriqui, L., Biedermann, E., Heffernan, J., Livings, R., Goodlet, B., and Mazdiyasni, S., 2018, "Uncertainty Quantification of Resonant Ultrasound Spectroscopy for Material Property and Single Crystal Orientation Estimation on a Complex Part," AIP Conf. Proc., **37**(44th Annual Review of Progress in Quantitative Nondestructive Evaluation, Volume), p. 140010.
[13] Heffernan, J., Jauriqui, L., Biedermann, E., Mayes, A., Livings, R., Goodlet, B., and Mazdiyasni, S., 2017, "Process Compensated Resonance Testing Models for Quantification of Creep Damage in Single Crystal Nickel-Based Superalloys," Mater. Eval., **75**(7), pp. 941–952.
[14] Heffernan, J., Biedermann, E., Mayes, A., Livings, R., Jauriqui, L., Goodlet, B., Aldrin, J. C., and Mazdiyasni, S., 2018, "Detection and Quantification of Creep Strain Using Process Compensated Resonance Testing (PCRT) Sorting Modules Trained With Modeled Resonance Spectra," AIP Conf. Proc., **37**(44th Annual Review of Progress in Quantitative Nondestructive Evaluation), p. 140006.
[15] Mayes, A., Jauriqui, L., Biedermann, E., Heffernan, J., Livings, R., Aldrin, J. C., Goodlet, B., and Mazdiyasni, S., 2018, "Part-to-Itself (PTI) Model Inversion in Process Compensated Resonance Testing (PCRT)," AIP Conf. Proc., **38**(45th Annual Review of Progress in Quantitative Nondestructive Evaluation), p. 020019.
[16] Iman, R. L., Davenport, J. M., and Zeigler, D. K., 1980, *Latin Hypercube Sampling (Program User's Guide)*, Sandia Laboratories and Texas Tech University, Albuquerque, NM.
[17] ASTM Standard E8, 2021, "Standard Test Method for Tension Testing of Metallic Materials," ASTM International, www.astm.org
[18] Lee, Y. T., and Welsch, G., 1990, "Young's Modulus and Damping of Ti-6AL-4V Alloy as a Function of Heat Treatment and Oxygen Concentration," Mater. Sci. Eng. A, **128**(1), pp. 77–89.
[19] Sonne, H. M., 1999, Bestimmung des Elastizitätsmoduls im Zugversuch; "Determination of Young's modulus in tensile testing. Tagung" Werkstoffprüfung, Vortrags- und Diskussionstagung, Bad Nauheim, Friedberg, Germany, pp. 219–230.
[20] Kostić, S., Miljojkovic, J., Simunovic, G., Vukelic, D., and Tadic, B., 2021, "Uncertainty in the Determination of Elastic Modulus by Tensile Testing," Eng. Sci. Technol. J., **25**.
[21] Antonysamy, A., Meyer, J., and Prangnell, P. B., 2013, "Effect of Build Geometry on the β-Grain Structure and Texture in Additive Manufacture of Ti-6AL-4V by Selective Electron Beam Melting," Mater. Charact., **84**, pp. 153–168.
[22] ASTM E3081, 2021, "Standard Practice for Outlier Screening Using Process Compensated Resonance Testing Via Swept Sine Input for Metallic and Non-Metallic Parts," ASTM International, www.astm.org